IEEE Photonics Journal
An IEEE Photonics Society Publication

Wideband Rapidly Tunable Delay-Controlled Optoelectronic Oscillator

Volume 12, Number 6, December 2020

Pouria Sanjari, *Student Member, IEEE*
Firooz Aflatouni, *Senior Member, IEEE*

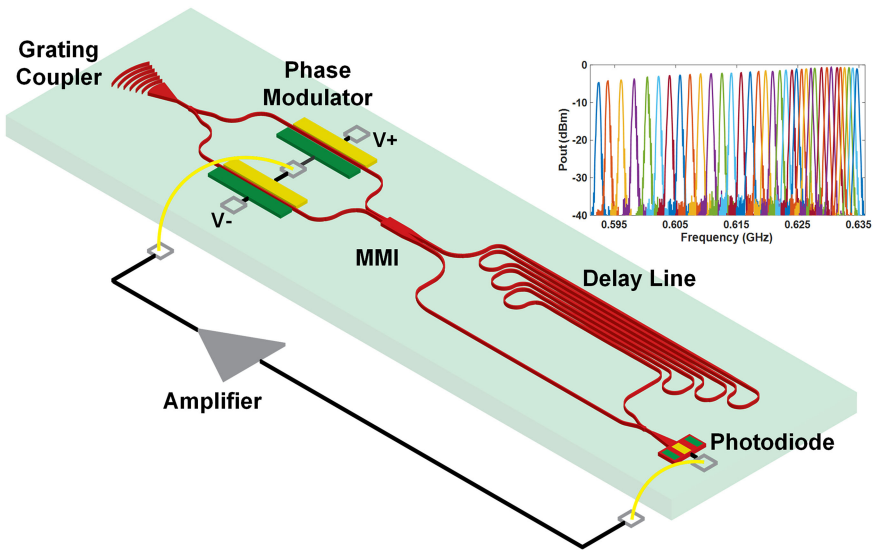

DOI: 10.1109/JPHOT.2020.3030613

Wideband Rapidly Tunable Delay-Controlled Optoelectronic Oscillator

Pouria Sanjari, ***Student Member, IEEE***,
and Firooz Aflatouni, ***Senior Member, IEEE***

Department of Electrical and Systems Engineering, University of Pennsylvania, Philadelphia, PA 19104 USA

DOI:10.1109/JPHOT.2020.3030613

Manuscript received September 15, 2020; revised October 6, 2020; accepted October 8, 2020. Date of publication October 13, 2020; date of current version November 6, 2020. Corresponding author: Pouria Sanjari. (e-mail: pouria@seas.upenn.edu).

Abstract: With the recent advancements in photonic integrated circuits, integrated RF photonics has increasingly been considered as a viable avenue to meet the demands of many emerging applications in telecommunication, sensing and signal processing. In this paper, an integrated, rapidly tunable, wideband optical delay line is used to implement an optoelectronic oscillator that can be continuously tuned from 594 MHz to 634 MHz. The oscillator exhibits a relatively flat modulation response at high frequencies (larger than 400 MHz), accommodating wideband fast frequency chirp generation with applications in radar and imaging. The on-chip variable delay line is characterized by continuously delaying an ultra-wide band 0.5–5 GHz monocycle pulse between 0–100 ps. The photonic integrated chip consists of silicon nanowaveguides, phase modulators, multimode interference coupler, a Mach-Zehnder interferometer, and a photodiode. The chip is fabricated on IME 180 nm Silicon Photonics platform and has an area of 0.55 mm^2.

Index Terms: Integrated optoelectronics, oscillators, optical delay.

1. Introduction

The field of RF photonics has enabled applications that would otherwise be challenging to realize with conventional conventional electronic circuitry. In RF photonics, inherent properties of photonic platforms are leveraged in order to implement high performance optoelectronic systems. In certain beamformers [1] and radar systems [2], optical delay lines replace electrical delay lines as they have significantly lower loss, higher bandwidth, are more immune to electromagnetic interference, and, in integrated cases, occupy a much smaller chip area for the same delay. Optoelectronic oscillators (OEO) [3] are another class of systems where photonic techniques have been employed to generate either low phase noise [4], low drift [5], highly tunable [6] or linearly chirped [7], [8] RF signals.

Despite their excellent performance, the widespread adoption of the above mentioned approaches have often been limited given that they are mostly benchtop systems requiring bulky components and or materials that are not conducive to integration. However, with the advancement of CMOS compatible photonic integrated circuits (PICs), many designers are aiming to benefit from photonic assisted electronics while simultaneously enjoying the associated advantages of integration such as miniaturization, lower cost and scalability. A few successful examples include

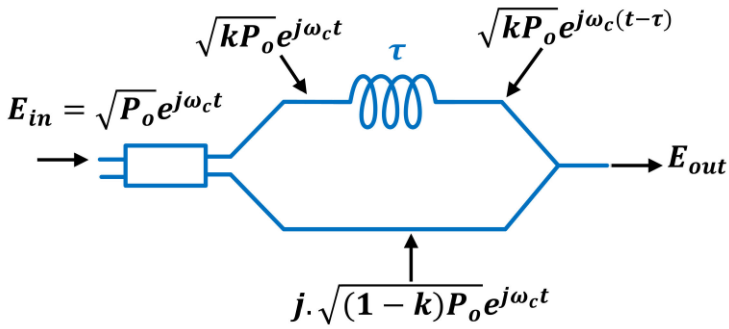

Fig. 1. Mach Zehnder Interferometer

an integrated imager [9] implemented using nanophotonic delay elements, and partially integrated beamformers with tunable optical delay lines based on cascaded ring resonators [10] and Mach-Zehnder Interferometers [11]. Similarly, OEOs integrated on platforms such as Silicon on Insulator (SOI) and Indium Phosphide [12]–[14] have previously been reported. In [12], a thermally tunable OEO, based on micro disk resonators, was shown to have a frequency range of 3-8 GHz. In [14], a hybrid integrated OEO with a dispersive delay line was used to frequency lock a laser to a RF oscillator.

In this paper, a rapidly tunable wideband optical delay line PIC is used to form a delay-controlled OEO which can be continuously tuned from 594 MHz to 634 MHz and has a relatively flat modulation response at high frequencies (larger than 400 MHz) corresponding to more than 65% modulation bandwidth to center frequency ratio. Typically, frequency tuning in OEOs is achieved by utilizing a frequency selective component that is either thermally [6], [12] or mechanically [3] adjusted, or by changing the wavelength of the laser through current injection [13]. Our proposed architecture utilizes photonic phase modulators (part of the variable delay line and used to close the loop) to change the group delay and hence the oscillation frequency. The advantage here is that, for applications involving oscillator modulation, we are no longer limited by low bandwidth mechanisms such as the FM response of the laser or the relatively slow thermal process. Given the large modulation bandwidth approaching the oscillator frequency, the proposed approach has potential applications in continuous-wave frequency modulated (FMCW) radar systems, imagers, and FMCW LiDARs.

The tunable delay line PIC used as part of the OEO is similar to [15]. The PIC is comprised of silicon nanowaveguides, phase modulators, multimode interference (MMI) coupler, Mach-Zehnder Interferometer (MZI), and a photodiode. To verify its functionality, the tunable delay line PIC is separately used to delay an UWB pulse. In this case, the group delay experienced by the input optical signal, modulated with a monocycle pulse with a bandwidth of 0.5–5 GHz, can be tuned from 0 to 100 ps equivalently delaying the detected UWB pulse. Such a tunable optical delay line has applications ranging from high speed equalization in photonic links [16] to optical coherence tomography [17] and photonic assisted beamformers [1], [9], [11].

2. Theory of Operation

Consider the MZI shown in Fig. 1 with a delay difference of τ between its arms. Assume the laser electric field at the input of the MZI is written as $\sqrt{P_o}\exp(j\omega_c t)$, where P_o and ω_c are the power and frequency of the optical wave, respectively. If kP_o is the amount of light coupled to the top arm, then assuming a lossless symmetric coupler, the amount of light in the bottom branch is given by $(1-k)P_o$, where k is the power coupling factor of the coupler. If the light in the top arm is delayed by τ and combined with the bottom arm through a Y-junction, the electric field at the output of the

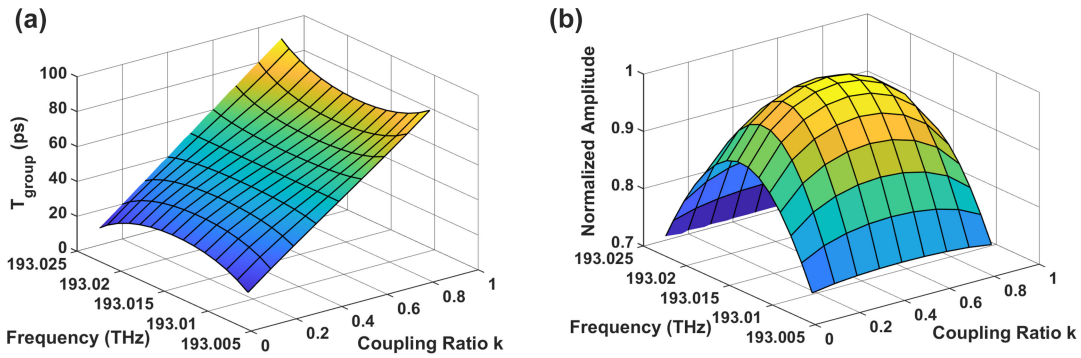

Fig. 2. (a) Group delay (b) Amplitude of the electric field at the output of the MZI vs frequency and coupling ratio.

MZI can be expressed as

$$E_{out} = \sqrt{\frac{P_0}{2}}.\sqrt{1-2\sqrt{k(1-k)}\sin(\omega_c\tau)}.\exp\left[j\omega_c\left(t-\frac{\tau}{2}\right)+j\left(\theta+\frac{\pi}{4}\right)\right], \quad (1)$$

where $\theta = \tan^{-1}[\kappa.\tan(\frac{\omega_c\tau}{2}+\frac{\pi}{4})]$ and $\kappa = (\sqrt{1-k}-\sqrt{k}).(\sqrt{1-k}+\sqrt{k})^{-1}$.

In this case, the MZI group delay can be calculated as

$$T_{group}(\omega_c) = -\frac{d\phi}{d\omega} = \frac{\tau}{2} - \frac{\frac{\tau}{2}\kappa\sec^2\left(\frac{\omega_c\tau}{2}+\frac{\pi}{4}\right)}{\kappa^2\tan^2\left(\frac{\omega_c\tau}{2}+\frac{\pi}{4}\right)+1}, \quad (2)$$

where $\phi = \theta + \frac{\pi}{4} - \frac{\omega_c\tau}{2}$.

Fig. 2(a) shows the group delay, (2), as a function of optical frequency and the MZI coupling ratio for a fixed delay τ of 100 ps. As evident from this plot, the group delay increases as the coupling ratio increases. Thus, by controlling the coupling ratio, the group delay experienced by the signal can be adjusted. Sections 3.1 and 4.2 discuss and demonstrate how two phase modulators and a MMI coupler form the input network of the MZI and control the coupling ratio. Note that, inherently, there is a tradeoff between the maximum achievable group delay and bandwidth. Specifically, as τ increases, the FSR of the MZI decreases and the bandwidth over which a relatively constant group delay can be achieved decreases. Fig. 2(b) shows the amplitude variations of the electric field as the frequency and coupling ratio are varied, where the amplitude variations remain under 30%.

3. System Architecture

3.1 Tunable Optical Delay Line

The architecture of the rapidly tunable wideband delay line is shown in Fig. 3. Light from a laser is coupled into the PIC through the grating coupler. A Y-junction splits the power into two branches leading to the inputs of a 2 × 2 MMI coupler. A p-n phase modulator [18] is placed in each branch to control the phase of the optical waves entering the MMI forming a 2-element phased array in silicon. The phase adjustment is performed by setting voltages V_1 and V_2. The phase adjusted optical waves interfere inside the MMI [19]. Depending on the relative phase between the two optical waves entering the MMI, the interference pattern, emulating a beam of light in silicon, can be steered and used to change the amount of light coupled to each output of the MMI. In this case, the MMI together with the phase modulators enable the rapid changing of the coupling ratio and hence, the signal group delay. After the MMI, light enters the MZI where it is combined with its delayed version. Finally, a photodiode is used to convert the optical signal back to the electrical domain. Use of high bandwidth p-n phase modulators (larger than 20 GHz) enables rapid coupling adjustments (and hence group delay control) which is more than 4 orders-of-magnitude faster

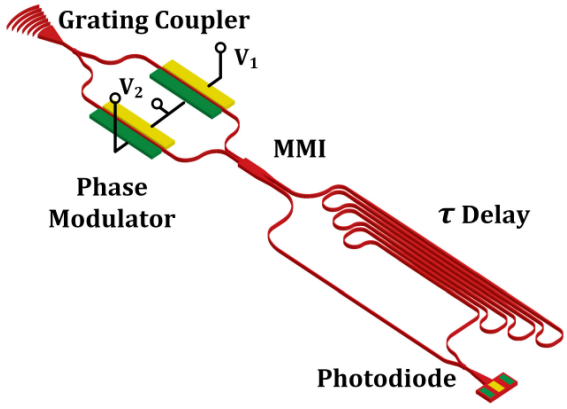

Fig. 3. Architecture of the rapidly tunable wideband delay line.

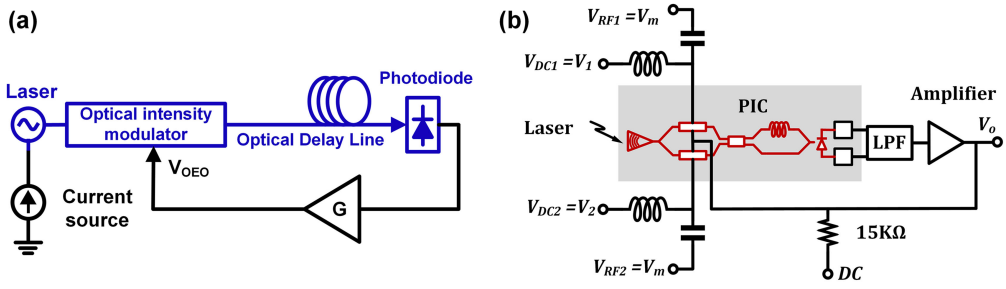

Fig. 4. (a) Block diagram of a conventional OEO. (b) Schematic of the proposed OEO.

compared to thermo-optic phase shifters. Furthermore, since the p-n phase modulators operate in reverse biased mode, the static power consumption, which is due to the leakage current of a reverse biased diode, is significantly lower when compared to p-i-n phase modulators (which are forward biased) and thermo-optic phase shifters.

3.2 Delay Controlled Optoelectronic Oscillator

A direct application of such a rapidly tunable delay element is to implement a delay-controlled oscillator. Fig. 4(a) shows the block diagram of a conventional OEO, where the output of a laser is intensity modulated, optically delayed, and photodetected. The photodiode output current is amplified and fed back to the intensity modulator. The oscillation frequency of such an OEO is set by the loop delay and is written as [3]

$$f_{OEO} = \begin{cases} \dfrac{k}{\tau_{total}}, & for\ G > 0 \\ \dfrac{2k+1}{2\tau_{total}}, & for\ G < 0 \end{cases}, \tag{3}$$

where τ_{total}, G and k are the total loop delay (in both electrical and optical domains), the total loop gain, and a non-negative integer, respectively. Self-sustained oscillation occurs for a large enough loop gain. Based on (3), the frequency of an OEO may be tuned by adjusting the loop delay.

Fig. 4(b) shows the block diagram of the proposed tunable OEO, where the rapidly tunable delay line PIC, forming part of the total loop delay, is used for OEO frequency tuning. In the proposed OEO, the loop delay consists of the group delay of the integrated tunable delay line, the group delay of the filter, loop amplifier, and the delay of the interconnects between the photonic chip and the

off-chip loop amplifier. In this case, the OEO frequency can be tuned by adjusting the DC biasing of the phase modulators which vary the group delay of the tunable optical delay line. The tuning range is determined by the portion of the total loop delay formed by the integrated tunable delay line. An important advantage of the implemented OEO is its capability to be modulated with high frequencies due to the use of the wideband phase modulators.

When the OEO in Fig. 4(b) is modulated by injecting a RF small signal to the phase modulators, there are two main mechanisms affecting the generation of sidebands around the free-running frequency.

3.2.1) Loop Delay Modulation: The first mechanism is the loop delay modulation. This effect is similar to the response of a voltage-controlled oscillator to a small signal modulation of its control voltage [20]. In this case, when the bias nodes are used to modulate the OEO, the output of the OEO can be expressed

$$V_{OEO} = V_o.\cos\left[2\pi f_o t + \frac{V_m.K(f_m)}{f_m}\cos(2\pi f_m t)\right], \tag{4}$$

where V_o, f_o, V_m, f_m, and $K(f_m)$ are the amplitude of the free running OEO, the fundamental frequency of the OEO, the amplitude of the modulating RF signal, the frequency of the RF modulating signal and the gain of the oscillator, respectively. By applying the Jacobi-Anger expansion [21] to (4), it can be shown that the amplitude of the fundamental tone is equal to $V_o.J_o(\frac{V_m.K(f_m)}{f_m})$ and the amplitude of the first sideband, $\cos[2\pi(f_o \pm f_m)]$, is written as

$$A_{DM,f_o\pm f_m} = V_o.J_1\left(\frac{V_m.K(f_m)}{f_m}\right), \tag{5}$$

where $A_{DM,f_o\pm f_m}$ represents the sideband amplitude due to small-signal delay modulation and J_o and J_1 are the 0^{th} and 1^{st} order Bessel functions of the first kind, respectively.

3.2.2) In Loop Optical Phase Modulation: The second mechanism affecting side band generation is the in-loop optical phase modulation of the light through the high bandwidth p-n phase modulators. In this scenario, similar to an intensity modulator, there will be frequency components at the output of the photodiode at $\cos[2\pi(f_o \pm f_m)]$ whose amplitudes can be approximated as

$$A_{PM,f_o\pm f_m} = \eta.C.J_1\left(\frac{2V_m}{V_\pi}\pi\right).J_1\left(\frac{2V_o}{V_\pi}\pi\right), \tag{6}$$

where $A_{PM,f_o\pm f_m}$ is the amplitude of the sidebands due to the direct small-signal phase modulation, V_π is the voltage required to introduce a π radians optical phase shift across the p-n phase modulator, C is determined by the laser power P_o, photodiode responsivity R, trans-impedance gain G_{TIA}, and the effective loss α, and $\eta \leq 1$ is a fitting parameter capturing the effects of the bias conditions of the MZI and MMI [3]. Given that the modulators have a large bandwidth (larger than 20 GHz), the sideband amplitude $A_{PM,f_o\pm f_m}$ is almost independent of the modulating frequency. Fig. 5 shows the calculated sideband power generated due to small-signal optical delay modulation, direct small-signal phase modulation of light, and the combined effects. At low modulation frequencies, the sideband power is dominated by the delay modulation and drops as $J_1(f_m{}^{-1})$ with increasing frequency as predicted by (5), whereas at higher modulation frequencies the sideband power is dominated by the direct phase modulation and plateaus as given by (6). As a result, compared to an electrical VCO, larger sideband power can be achieved at higher modulation frequencies using the OEO system.

4. Characterization of Photonic Components

4.1 Mach Zehnder Interferometer

In order to characterize the MZI forming part of the variable delay line, the wavelength of the input laser was swept and the output photocurrent was measured. For a coupling ratio of 50%, the

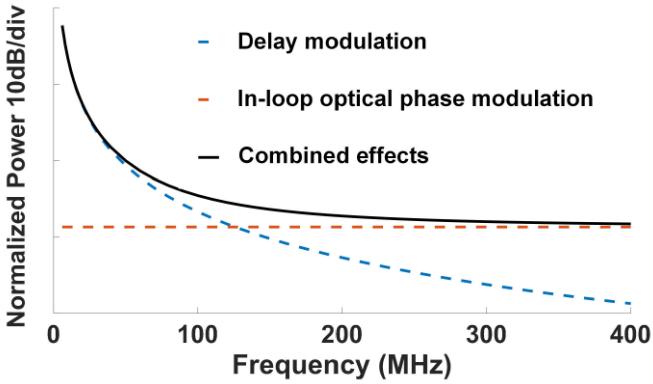

Fig. 5. Sideband power vs increasing modulation frequency as predicted by (5) and (6) ($V_\pi = 9$ V, $V_O = 1.8$ V, $V_m = 0.065$ V, K = 25 MHz/V, $\eta = 1$, C = 1. Actual measurement conditions (η and C) discussed in Section 5).

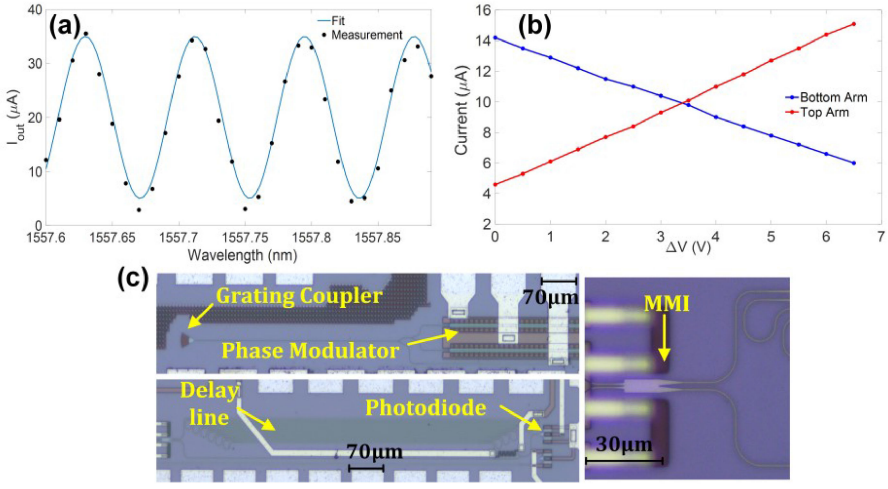

Fig. 6. (a) Response of the MZI forming part of the variable delay line. (b) The performance of the coupling control mechanism. (c) Microphotograph of the tunable delay line chip showing the grating coupler, phase modulators, MZI, photodiode and MMI.

photocurrent at the output of the variable delay line can be written as

$$I_{out} = R.\left[\left(\frac{P_o}{2} + \frac{P_o}{2}\cos(\omega_c \tau)\right)\right], \tag{7}$$

where R is the responsivity of the photodiode. Fig. 6(a) shows the measured response of the tunable delay line when the coupling ratio is set to 50%, which is compared with Eq. (7) for a delay of τ =100 ps.

4.2 Multimode Interference Coupler and Reverse Biased p-n Phase Modulators

A test structure was used to measure the coupling adjustment performance. To do this, the power in the output arms of the MMI was monitored while the voltages across the phase modulators were changed. Fig. 6(b) shows the photocurrent in the top and bottom arm of the MMI as the drive voltage of the two phase shifters $\Delta V = V_1 - V_2$ is varied. As shown in Fig. 6(b), by changing the voltage across the modulators, the amount of light directed to the output arms of the MMI can

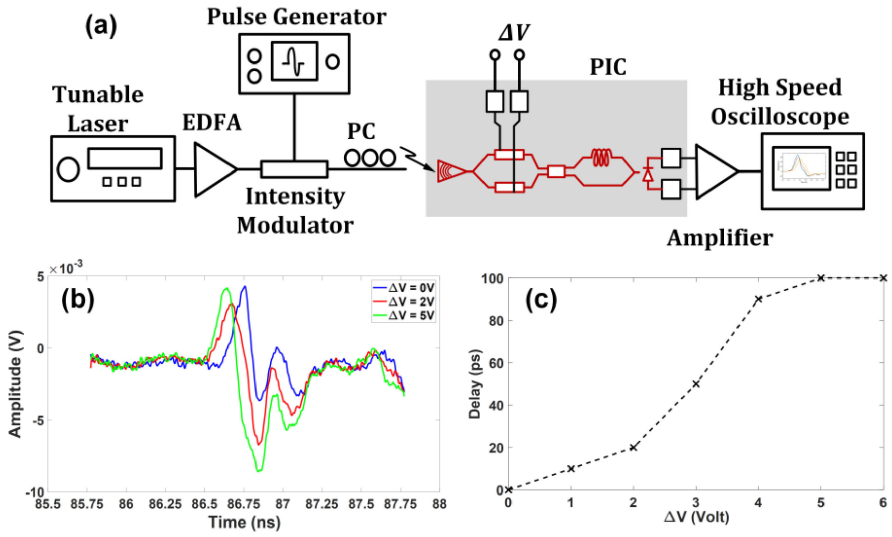

Fig. 7. (a) Measurement setup showing the tunable laser amplified by an EDFA, intensity modulated by the pulse generator and coupled into the PIC using a polarization controller (PC) and an optical probe. An amplifier and high speed oscilloscope are used to monitor the photodetected UWB electrical signal. (b) UWB monocycle pulse delayed using the photonic assisted tunable delay line chip. (c) Pulse delay vs voltage applied across the phase modulators.

be adjusted. Note that in the above measurements, during the 0 V bias condition of the phase modulators, there may be a relative phase difference between the optical waves at the inputs of the MMI resulting in a coupling ratio that is not 50/50. This is most likely due to process variation in the doped nanowaveguides of the phase modulators. Furthermore, a power imbalance in the input arms of the MMI, primarily due to different reverse biases across the p-n phase modulators, may also adversely affect the coupling performance. The loss of the phase modulators is measured to be around 5 dB for a 2 mm section. The microphotograph of the various parts of the characterized photonic integrated chip is shown in Fig. 6(c).

5. Measurement Setup and Experimental Results

Fig. 7(a) shows the setup used to measure the standalone performance of the integrated variable delay line. An Agilent 81642A tunable laser at 1557 nm was amplified using an EDFA (5 dB noise figure) and intensity modulated by a 0.5–5 GHz UWB monocycle pulse. The modulated light was then coupled into the chip through the grating coupler using an optical probe. Voltages across the phase modulators were varied to change the delay setting. An on-chip photodiode with a bandwidth larger than 15 GHz was used to down-convert and detect the delayed UWB pulse. This down-converted electrical signal was then amplified and monitored on a high speed oscilloscope. The time domain waveforms of the delayed monocycle for various voltage settings are shown in Fig. 7(b), where about 100 ps delay adjustment is demonstrated. Note that, as previously discussed and shown in Fig. 1(c), delay adjustments also affect the amplitude of the signal. Fig. 7(c) summarizes the achieved delay vs the applied voltage across the phase modulators.

Fig. 8(a) shows the measurement setup used to characterize the delay-controlled OEO. The tunable laser was amplified to about 12 dBm using an EDFA and coupled into the chip using an optical probe. A 45 dB amplifier was used to close the loop while a low pass filter with a cut-off frequency of 2.3 GHz (which is much higher than the operating frequency) was used to suppress higher harmonics and to reduce the effect of PCB leakage at high frequencies. Fig. 8(b) shows the measured spectrum of the OEO output where the fundamental frequency of the OEO was tuned

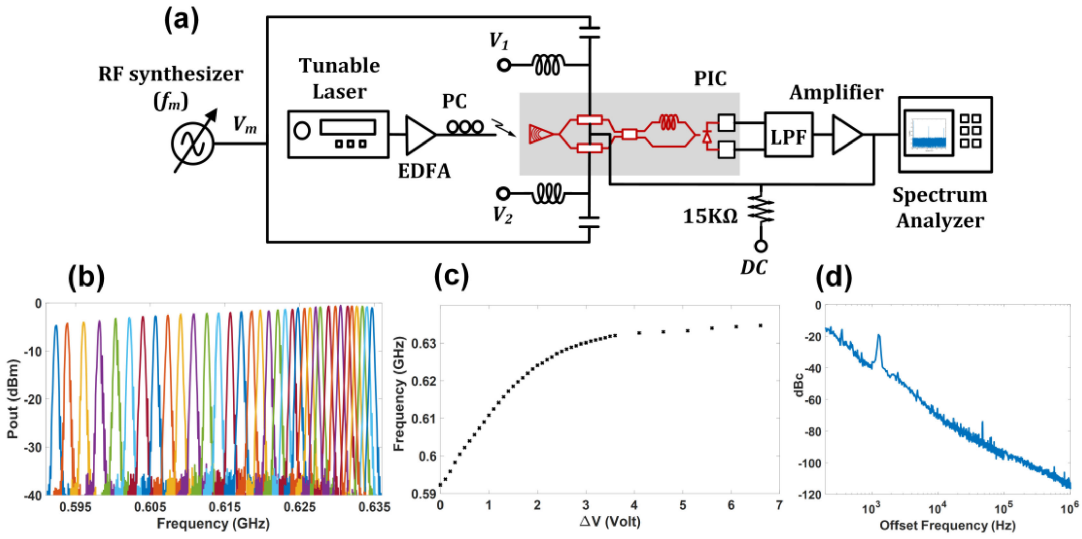

Fig. 8. (a) Measurement setup of the OEO where $V_1 - V_2 = \Delta V$ is used to tune the frequency and V_m is used to modulate the OEO. (b) Superimposed RF spectrums of the OEO. (c) OEO frequency gain (with a maximum sensitivity of 25 MHz/V in the linear region). (d) Phase noise of the OEO when operating at 600 MHz.

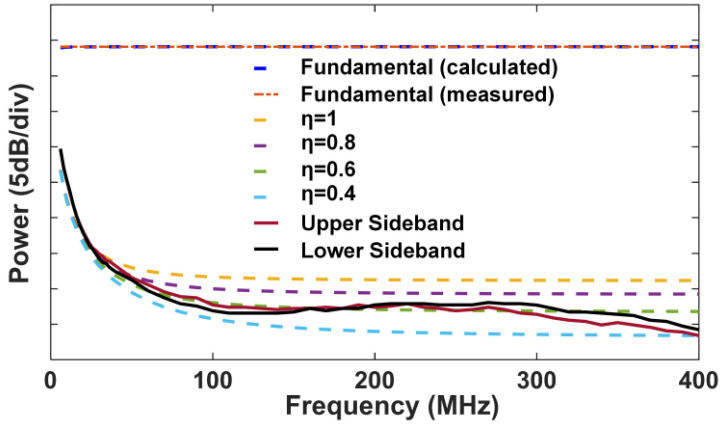

Fig. 9. Variation in the power of the sidebands and fundamental tone as the modulating frequency f_m is swept along with their respective fits (P_o = 8dBm, R = 0.9, G_{TIA} = 5 kΩ, V_π = 9 V, V_O = 1.8 V, α = 4, K = 25 MHz/V).

by adjusting the DC biasing of the phase modulators to change the loop delay. A frequency shift from 594 MHz to 634 MHz corresponds to a delay change of about 106 ps, which is in agreement with the response of the MZI. Additionally, the phase noise of the OEO was measured to be around −115 dBc/Hz at 1 MHz offset when operating at 600 MHz.

Fig. 9 shows the measured power of the fundamental tone and first sideband for small signal modulation of the OEO as the modulation frequency is swept. The respective fits using the combined effects of (5) and (6), measurement condition, and extracted parameters are also specified. Note that since the initial optical phase difference between the two inputs of the MMI and also the initial optical phase difference between the two arms of the MZI are unknown, four different plots corresponding to different bias conditions (corresponding to a range of initial phases) are depicted. As evident, the amplitudes of the sidebands decay as $J_1(f_m^{-1})$ for frequencies up to 100 MHz and

tend to plateau at higher frequencies. These effects combine to yield an OEO with a large effective modulation bandwidth. Note that since typical OEOs utilize phase or intensity modulators to close the loop, high frequency injection to the OEO may be possible, but not high frequency modulation. In order to frequency tune the OEO, these systems often either inject current to the input laser [13] or have a separate frequency selective component, such as a filter that is thermally [6], [12] or mechanically [3] adjusted. In our particular implementation, since the phase modulators are high speed optical components and responsible for frequency tuning, the OEO has a large effective modulation bandwidth.

6. Conclusion

An optoelectronic oscillator with a continuous tuning range of 594 MHz to 634 MHz, capable of being modulated with frequencies as high as 400 MHz, was implemented using an integrated wideband rapidly tunable optical delay line. The oscillator utilizes high bandwidth phase modulators to control the group delay and hence the oscillation frequency thus avoiding low bandwidth mechanisms such as the FM response of the laser or the thermo-optic effect which are often involved when tuning the frequency of an optoelectronic oscillator. The integrated tunable delay line, which consists of a MZI, phase modulators, MMI coupler and a photodiode, was separately characterized by delaying a 0.5–5 GHz UWB monocycle pulse from 0 to 100 ps.

References

[1] H. Zmuda, R. A. Soref, P. Payson, S. Johns, and E. N. Toughlian, "Photonic beamformer for phased array antennas using a fiber grating prism," *IEEE Photon. Technol. Lett.*, vol. 9, no. 2, pp. 241–243, Feb. 1997.

[2] A. Wang *et al.*, "Ka-band microwave photonic ultra-wideband imaging radar for capturing quantitative target information," *Opt. Express*, vol. 26, no. 16, pp. 20708–20717, Aug. 2018.

[3] S. Yao and L. Maleki, "Optoelectronic microwave oscillator," *J. Opt. Soc. America B.*, vol. 13, no. 8, pp. 1725–1735, Aug. 1996.

[4] D. Eliyahu, D. Seidel, and L. Maleki, "Phase noise of a high performance OEO and an ultra-low noise floor cross-correlation microwave photonic homodyne system," in *Proc. IEEE Int. Freq. Control. Symp.*, May 2008, pp. 811–814.

[5] S.E. Hosseini, A. Banai, and F. X. Kartnet, "Low-drift optoelectronic oscillator based on a phase modulator in a sagnac loop," *IEEE Trans. Microw. Theory Techn.*, vol. 65, no. 7, pp. 2617–2624, Jul. 2017.

[6] X. Xie *et al.*, "Wideband tunable optoelectronic oscillator based on a phase modulator and a tunable optical filter," *Opt. Lett.*, vol. 38, no. 5, pp. 655–657, Mar. 2013.

[7] L. Zhuang *et al.*, "Generation of linear frequency-modulated waveforms by a frequency-sweeping optoelectronic oscillator," *J. Lightw. Technol.*, vol. 36, no. 18, pp. 3927–3934, Sep. 2018.

[8] T. Hao *et al.*, "Breaking the limitation of mode building time in an optoelectronic oscillator," *Nat. Commun*, vol. 9, May 2018, Art. no. 1839.

[9] F. Ashtiani, A. Risi, and F. Aflatouni, "Single-chip nanophotonic near-field imager," *Optica*, vol. 6, no. 10, pp. 1255–1260, Oct. 2019.

[10] L. Zhuang *et al.*, "Novel ring resonator-based integrated photonic beamformer for broadband phased array receive antennas-part II: Experimental prototype," *J. Lightw. Technol.*, vol. 28, no. 1, pp. 19–31, Jan. 2010.

[11] V. C. Duarte *et al.*, "Integrated photonic true-time delay beamformer for a Ka-band phased array antenna receiver," in *Proc. Opt. Fiber Commun. Conf.*, San Diego, CA, 2018, Paper M2G.5.

[12] W. Zhang and J. Yao, "Silicon photonic integrated optoelectronic oscillator for frequency-tunable microwave generation," *J. Lightw. Technol.*, vol. 36, no. 19, pp. 4655–4663, Oct. 2018.

[13] J. Tang *et al.*, "Integrated optoelectronic oscillator," *Opt. Express*, vol. 26, no. 9, pp. 12257–12265, Apr. 2018.

[14] Z. Xuan, L. Du, and F. Aflatouni, "Frequency locking of semiconductor lasers to RF oscillators using hybrid-integrated opto-electronic oscillators with dispersive delay lines," *Opt. Express*, vol. 27, no. 8, pp. 10729–10737, Apr. 2019.

[15] V. C. Duarte, M. V. Drummond, and R. N. Nogueira, "Photonic true-time-delay beamformer for a phased array antenna receiver based on self-heterodyne detection," *J. Lightw. Technol.*, vol. 34, no. 23, pp. 5566–5575, Dec. 2016.

[16] B. Abiri, F. Aflatouni, and A. Hajimiri, "Self-equalizing photodiodes, a hybrid electro-optical approach to tackle bandwidth limitation in high-speed signaling," *Opt. Express*, vol. 25, no. 16, pp. 19137–19146, Aug. 2017.

[17] E. Choi, J. Na, S. Ryu, G. Mudhana, and B. Lee, "All-fiber variable optical delay line for applications in optical coherence tomography: Feasibility study for a novel delay line," *Opt. Express*, vol. 13, no. 4, pp. 1334–1345, Feb. 2005.

[18] A. Liu *et al.*, "High speed High-speed optical modulation based on carrier depletion in a silicon waveguide," *Opt. Express*, vol. 15, no. 2, pp. 660–668, Jan. 2007.

[19] L. B. Soldano and E. C. M. Pennings, "Optical multi-mode interference devices based on self-imaging: Principles and applications," *J. Lightw. Technol.*, vol. 13, no. 4, pp. 615–627, Apr. 1995.

[20] F. M. Gardner, in *Phaselock Techniques*. Hoboken, NJ, USA: Wiley, 2005.

[21] D. Colton and R. Kress, in *Inverse Acoustic and Electromagnetic Scattering Theory*. Berlin, Gemany: Springer, 2012, ch. 2.